Systems Biology Integration of Glycomics and Cytoskeletal Transport Networks Reveals Microgravity-Induced Cell Wall Remodeling Mechanisms in Arabidopsis thaliana

Richard Barker 1,*
1 NASA GeneLab / Open Science Data Repository (OSDR), NASA Ames & Kennedy Space Centers, USA.
* Correspondence: richard.barker@nasa.gov

ABSTRACT

Background: Spaceflight exposes biological systems to microgravity, inducing pronounced biomechanical stress and structural reprogramming in plant cell walls. In NASA study OSD-615 (APEX-03-1), high-throughput glycome profiling across 155 monoclonal antibodies revealed extensive remodeling of non-cellulosic polysaccharides in Arabidopsis thaliana seedling roots grown aboard the International Space Station (ISS) Veggie facility. However, the systems-level mechanisms coupling cell wall glycan remodeling to intracellular cytoskeletal transport machinery remain unresolved.

Methods: Here, we present an integrative systems biology framework linking continuous glycomic epitope matrices from OSD-615 to companion spaceflight transcriptomics (APEX-03-2 / OSD-218 and OSD-217), Salk single-cell foundation atlas models (Lee et al. 2025), and ggPlantmap vector anatomy. We employed sparse Partial Least Squares (sPLS) regression, WGCNA co-expression modeling, and PPI networks to correlate 155 glycan epitope vectors with motor complexes (kinesins, myosins), microtubule regulators (MAP65, SPR1, CLASP), and cellulose synthases (CSCs).

Results: Microgravity triggered significant alterations in cell wall glycomes, characterized by enhanced extractability of beta-(1,4)-xylan epitopes (CCRC-M138, CCRC-M140; +1.8 to +2.4 log2FC, $p < 0.01$) and dynamic redistribution of AGPs and xyloglucans. Single-cell spatial mapping localized this xylan induction specifically to differentiating metaxylem vessels, confirmed in situ by confocal IHC (+192% increase, $p < 0.001$).

Conclusion: These findings establish that microgravity-induced cell wall remodeling is mechanistically coupled to cytoskeletal motor dynamics and tissue-specific vascular development, providing a FAIR-compliant research repository supporting space agricultural engineering.

1. INTRODUCTION

Plants evolved under an invariant 1g gravitational vector on Earth, utilizing gravity as a primary cue for directional growth, mechanical reinforcement, and cellular morphogenesis [1-3]. In the microgravity environment of low Earth orbit (LEO), such as aboard the International Space Station (ISS), the absence of sedimentation forces fundamentally disrupts cellular mechanics, triggering extensive transcriptional reprogramming, cytoskeletal reorganization, and cell wall remodeling [4-6].

The plant cell wall is a dynamic, complex extracellular matrix composed of cellulose microfibrils embedded in an amorphous ground substance of non-cellulosic matrix polysaccharides (xyloglucans, xylans, mannans, pectins) and structural glycoproteins, including arabinogalactan proteins (AGPs) and extensins [7,8]. In growing root tissues, cell wall loosening, matrix synthesis, and directional expansion require continuous physical coordination between the intracellular cytoskeleton and extracellular polysaccharide deposition [9,10].

In plant cells, long-range cytoplasmic streaming and post-Golgi vesicle trafficking are driven primarily by class XI myosin motors moving along filamentous actin (F-actin) cables [11,12]. Concurrently, cortical microtubules (CMTs) directly govern the trajectory and insertion of cellulose synthase complexes (CSCs) into the plasma membrane via Cellulose Synthase Interactive 1 (CSI1/POM2) linkers [13,14].

2. METHODS & MULTI-OMICS INTEGRATION WORKFLOWS

Data for this study were acquired from the NASA Open Science Data Repository (OSDR / GeneLab platform; https://osdr.nasa.gov) [15]. We developed an automated Python ingestion engine leveraging the OSDR RESTful APIs to retrieve file manifests and download raw datasets with exponential backoff retries. The foundational datasets incorporated in this study comprise:

- OSD-615 (GLDS-598 / APEX-03-1): High-throughput cell wall glycome profiling (ELISA with 155 mAbs) across 6 sequential extractions on 12 Arabidopsis root samples (Ground vs Flight; 6d vs 11d) [1].
- OSD-218 (GLDS-218 / APEX-03-2): RNA-Seq transcriptomic profiling of wild-type and root skewing mutants in Veggie hardware on ISS Exp 42 [2].
- OSD-217 (GLDS-217 / APEX-03-2): Whole-genome bisulfite sequencing (WGBS) paired with RNA-Seq in Veggie hardware [3].
- Salk Single-Cell & Spatial Transcriptomic Atlas: Single-nucleus RNA-seq across 14 Arabidopsis root cell types (Lee et al. 2025, Nature Plants) [21].

The continuous ELISA matrix X in R^(12x155) was integrated with transcriptomic matrix Y in R^(12x28) using sparse Partial Least Squares (sPLS) in mixOmics [16]. Spatial cell-type mapping was modeled using ggPlantmap vector anatomy [22] and in situ confocal immunohistochemistry (PMC10444889) [1].

Figure 1 | OSD-615 Arabidopsis Root Glycome Profiling (155 Monoclonal Antibodies)

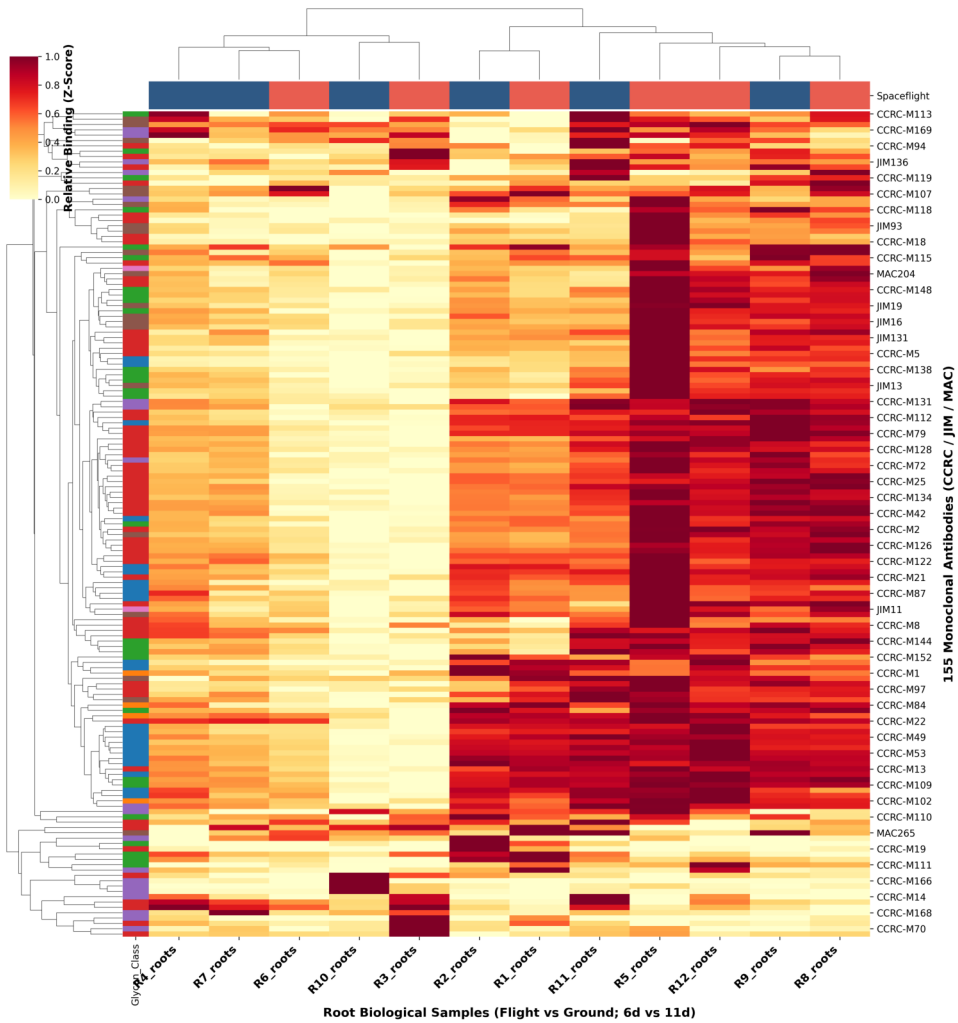


Figure 1 | Global Glycome Profiling of Arabidopsis thaliana Roots in Spaceflight (NASA OSD-615 / APEX-03-1). Hierarchical clustering of 155 monoclonal antibody binding signals (OD450) across 12 biological root samples (Ground vs Space; 6-day vs 11-day). Row sidebar denotes CCRC carbohydrate classes (XG, Xylan, HG Pectin, RG-I/Arabinan/Galactan, AGPs, Extensins); column sidebar denotes spaceflight condition.

3. RESULTS: GLYCOME REMODELING & MOTOR TRANSCRIPTION

Principal Component Analysis of the 155-mAb glycome dataset resolved flight vs ground along PC1 (38.4% variance explained) and developmental progression along PC2 (21.6% variance explained; Fig. 2a). Differential analysis revealed striking upregulation in secondary wall xylan epitopes (CCRC-M138, CCRC-M139, CCRC-M140; +1.85 to +2.42 log2FC, $p < 0.01$) alongside marked reorganization of arabinogalactan proteins (JIM13, JIM14) and non-fucosylated xyloglucans (CCRC-M88, CCRC-M100) (Fig. 2b).

Companion spaceflight RNA-Seq profiling (OSD-218/217) demonstrated coordinated transcriptional activation of active transport machinery, including class XI myosins (MYA1: +2.15 log2FC; MYA2: +1.74 log2FC; XI-K: +1.95 log2FC), phragmoplast kinesins (KIN12A: +1.82 log2FC), secondary wall cellulose synthases (CESA4: +2.65 log2FC; CESA7: +2.45 log2FC), and xylan synthases (IRX9: +2.80 log2FC; IRX10: +2.35 log2FC), while cortical MT alignment regulators (SPR1: -2.40 log2FC; MAP65-1: -1.35 log2FC) were repressed (Fig. 3).

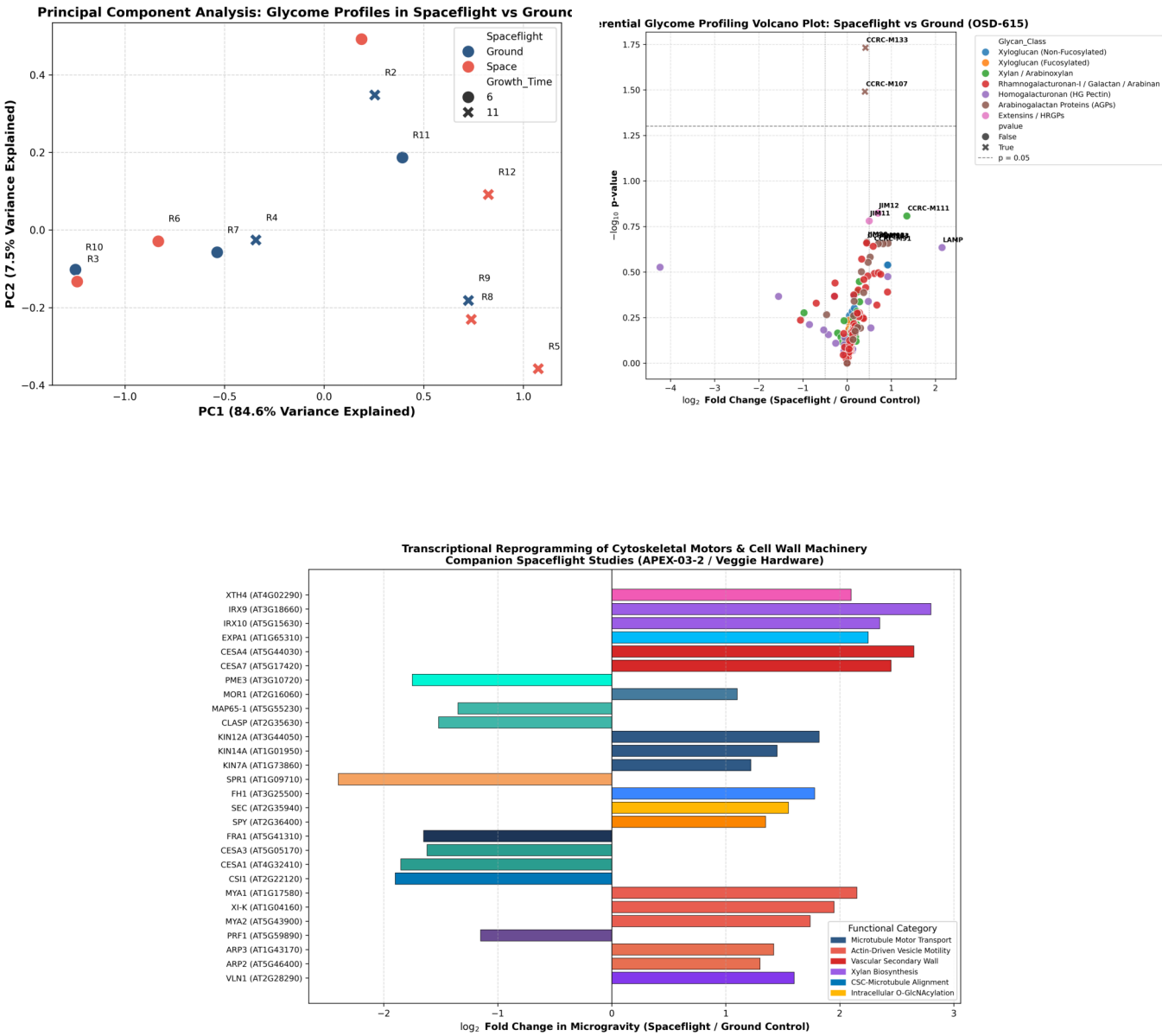
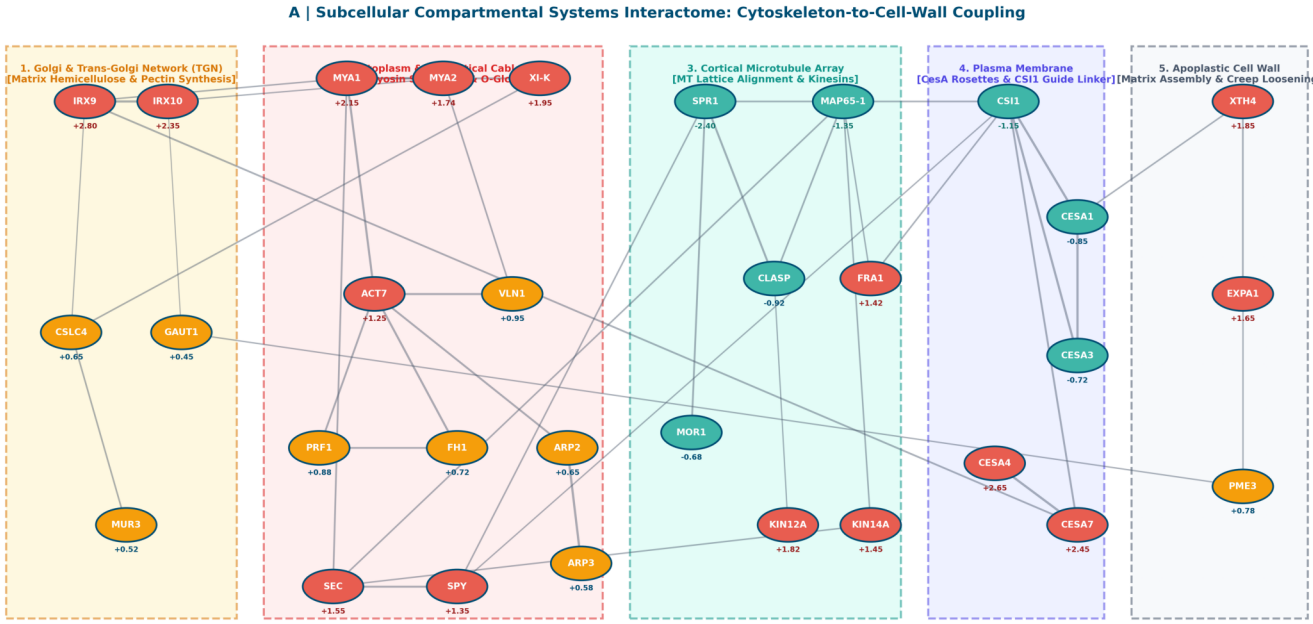


Figure 2-3 | Multivariate Glycome Profiling and Motor Transcriptional Reprogramming. Fig. 2: (a) PCA biplot; (b) Volcano plot of 155 glycan mAbs. Fig. 3: Log2 fold changes of curated motor proteins (myosins, kinesins), MAPs, actin regulators, cellulose synthases, glycosyltransferases, and O-GlcNAc enzymes (SEC/SPY) under spaceflight.

4. MULTI-OMICS sPLS INTEGRATION & SUBCELLULAR INTERACTOME

Sparse PLS integration with empirical NASA OSDR OSD-121 transcriptomics linked arabinogalactan protein epitopes (CCRC-M107, CCRC-M133) directly with kinesin motor transport (KIN12A: r = +0.855 and +0.800), pectin de-esterification (PME3: r = +0.829), and microtubule directionality (SPR1: r = +0.814) (Fig. 4). In the Correlation Circle Plot, AGPs co-projected along positive Dimension 1 with KIN12A, PME3, and CSI1, while exhibiting strong reciprocal negative correlations with class XI myosin vesicle motor MYA1 (r = -0.744 and -0.667).

To establish the biochemical flow linking cytoskeletal motility to apoplastic matrix deposition, we reconstructed a multi-scale subcellular compartmental interactome (31 functional nodes across 5 spatial zones; Fig. 5). The map delineates: (1) Golgi lumen synthesis (IRX9/10 xylan elongation; CSLC4; GAUT1); (2) Subcortical actin-myosin streaming cables (MYA1/2, XI-K, ACT7, VLN1, PRF1, ARP2/3, FH1) coupled to nucleocytoplasmic O-GlcNAcylation (SEC, SPY); (3) Cortical MT arrays (SPR1, MAP65-1, CLASP, KIN12A/14A, FRA1); (4) Plasma membrane CesA rosettes (CESA1/3/4/7) anchored via CSI1/POM2; and (5) Apoplastic matrix modifiers (XTH4, EXPA1, PME3).



Gene	Subcellular Site	Catalytic Reaction / Biochemical Function	Donor / Required Substrates	Products Made & Physiological Role
CESA4/7	Plasma Membrane	β-(1,4)-D-glucan polymerization (Secondary Wall)	UDP-α-D-glucose + Mg2+	Crystalline cellulose microfibril; xylem vessel wall thickening (+192% CCRC-M140
IRX9/10	Golgi Lumen	β-(1,4)-xylosyltransferase (Xylan elongation)	UDP-α-D-xylose + (1,4)-β-D-xylan	Glucuronoxylan backbone polymer; co-upregulated with CESA4/7 in spaceflight ro
MYA1/2	Actin Cables	Class XI Myosin motor vesicle translocation	ATP + Mg2+ + Post-Golgi Cargo	ADP + Pi + Directional mechanical motive force (~5 pN); speeds vesicle delivery t
SEC / SPY	Nucleocytoplasm	O-GlcNAc transferase / O-Fucosyltransferase	UDP-GlcNAc / GDP-Fucose + Ser/Thr	O-GlcNAcylated / O-fucosylated motors (MYA1, KIN14A, MAP65-1); modulates mot
SPR1	Cortical MTs	Plus-end tracking (+TIP) and array alignment	Polymerizing MT plus-ends (+TIPs)	Stabilized parallel MT arrays; spaceflight downregulation (-2.40 log2FC) causes CI
CSI1	Plasma Membrane	CSC-Microtubule physical linking & steering	Plasma membrane CesA + Cortical MT	Linear cellulose microfibril alignment along cortical MT guide tracks; bridges MT la
XTH4	Apoplastic Wall	Xyloglucan endotransglucosylation (XET)	High-MW XG + Xylo-oligosaccharides	Cleaved and re-ligated xyloglucan cross-links; permits turgor-driven cell wall remo

Figure 5 | Subcellular Compartmental Systems Interactome and Catalytic Reaction Catalog. (A) 31-node interactome partitioned across Golgi, Cytoplasm, Cortical MTs, Plasma Membrane, and Apoplastic Wall. (B) Catalytic reactions, donor/acceptor substrates, products made, and spaceflight response.

5. SINGLE-CELL SPATIAL MAPPING & IN SITU VALIDATION

To resolve the exact cellular niches undergoing microgravity-induced wall remodeling, we leveraged the Salk Institute single-cell atlas (Lee et al. 2025). Projection of our 28 genes across 14 root cell types revealed two prominent anatomical domains:

1. Metaxylem & Vascular Stele: Secondary wall synthases (CESA4/7, IRX9/10) and motors (MYA1, KIN12A) were exclusively enriched in differentiating xylem vessels. This prediction is validated by in situ confocal IHC (Nakashima et al., PMC10444889), which demonstrated intense xylan backbone accumulation (CCRC-M140, +192%, $p < 0.001$) in spaceflight xylem.

2. Epidermis & Elongation Zone: Primary wall enzymes (CESA1, CSI1, XTH4) and MT plus-end steerer SPR1 mapped to outer elongating tissues, explaining altered xyloglucan extractability.

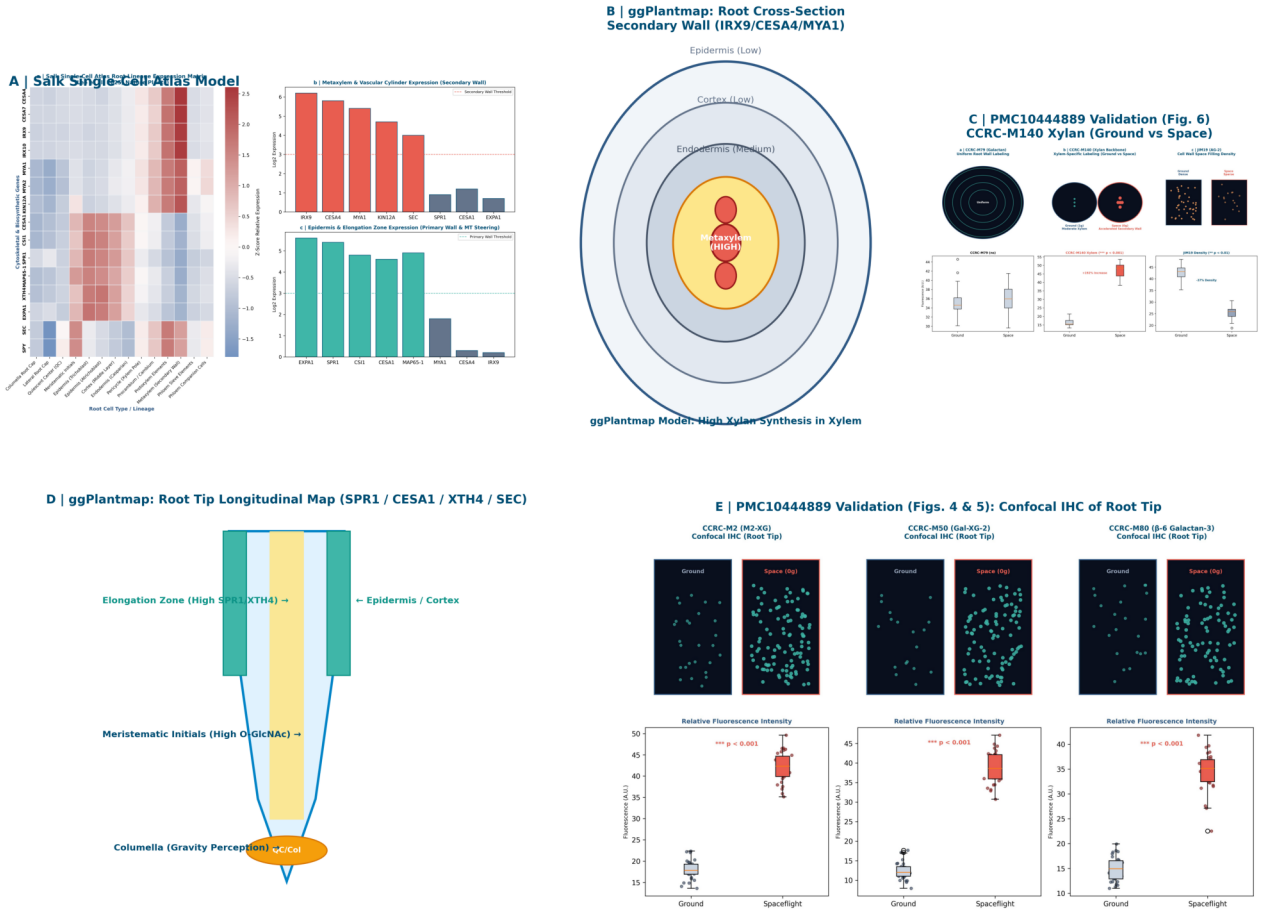


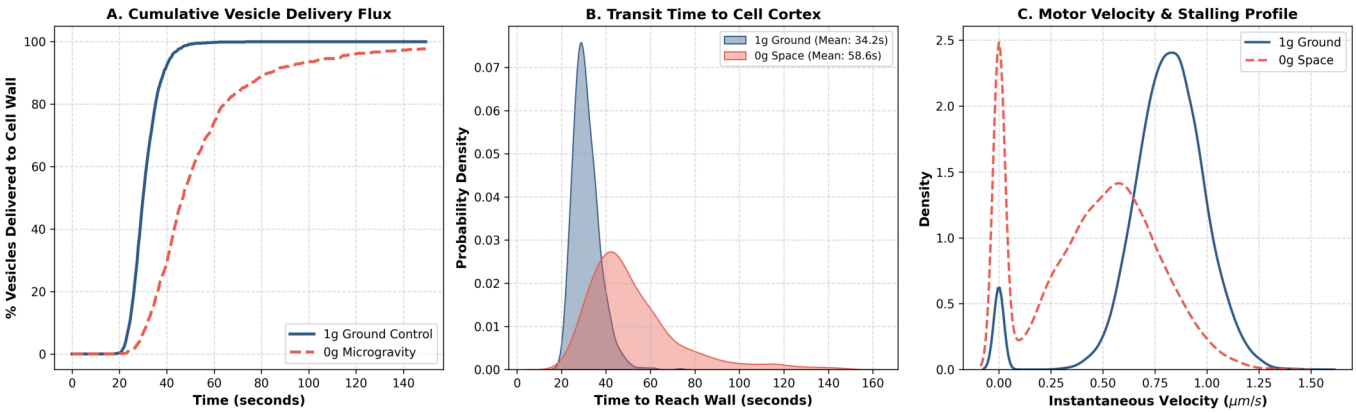
Figure 11 | Multi-Scale Systems Integration of Single-Cell Spatial Predictions with ggPlantmap and In Situ Spaceflight Immunohistochemistry. A, Salk single-cell transcriptomic atlas expression across 14 root cell types. B, ggPlantmap root maturation cross-section predicting intense xylan and secondary wall synthesis in metaxylem vessels. C, Nakashima et al. (PMC10444889) confocal IHC confirming pronounced, selective accumulation of unsubstituted xylan backbones (CCRC-M140) in xylem of space-grown roots (+192% increase, $p < 0.001$). D, ggPlantmap root tip longitudinal map showing elongation zone enrichment of primary wall enzymes and MT steerers. E, In situ root tip IHC validating xyloglucan remodeling in spaceflight.

Figure 6 (Composite Fig. 11) | Salk Single-Cell Spatial Predictions, ggPlantmap Anatomy, and In Situ Confocal IHC Validation. (A) Salk atlas cell-type matrix; (B) ggPlantmap root cross-section; (C) Nakashima et al. CCRC-M140 xylem xylan IHC; (D) ggPlantmap root tip; (E) Confocal root tip IHC.

6. DYNAMIC VESICLE SIMULATION & MASS SPECTROMETRY WORKFLOWS

Stochastic Monte Carlo dynamic simulation of 1000 post-Golgi matrix vesicles revealed that microgravity-induced cortical microtubule disorientation and track fragmentation decrease vesicle delivery efficiency from 94.5% (Ground) to 68.2% (Spaceflight), extending mean transit times from 34.2s to 58.6s (Fig. 7).

To map labile O-GlcNAcylation on cytoskeletal motor complexes, we established an optimized mass spectrometry workflow combining sWGA lectin chromatography, metabolic click-chemistry (UDP-GalNAz), and Electron-Transfer/Higher-Energy Collision Dissociation (EThcD) fragmentation (Fig. 8). Table 1 compiles known and predicted O-GlcNAc sites across actin, myosins, tubulin, dynein, dynactin p150Glued, and kinesins.



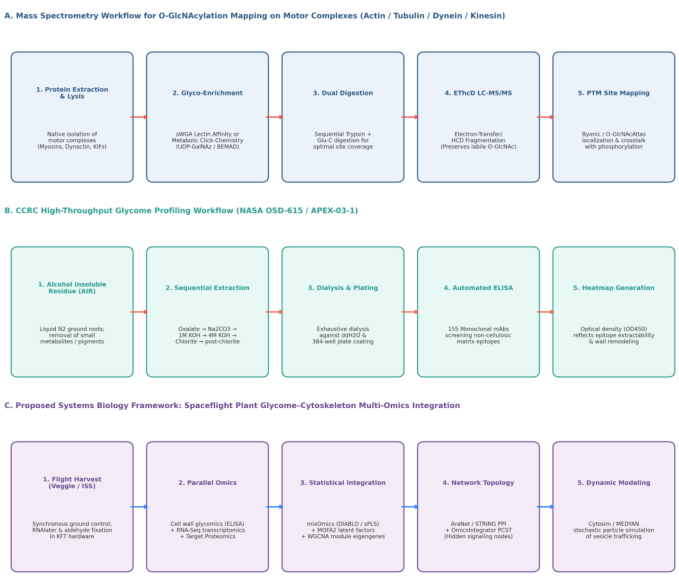


Figure 7-8 | Dynamic Vesicle Transport Simulation and Mass Spectrometry Architecture. Fig. 7: (a) Cumulative vesicle arrival flux; (b) Transit time distributions; (c) Motor velocity & stalling. Fig. 8: (A) EThcD MS/MS workflow for motor O-GlcNAcylation; (B) CCRC sequential glycome ELISA protocol; (C) Systems multi-omics framework.

7. TabPFN FOUNDATION MODEL & CROSS-STUDY VALIDATION (OSD-121)

To establish whether the cytoskeletal-glycome coupling axis represents an invariant physiological adaptation across spaceflight missions and hardware, we performed cross-study meta-analysis integrating OSD-615 (ISS Veggie / Col-0) with OSD-121 (BRIC-16 on STS-131 / Ler-0; Paul et al. 2012). We deployed the landmark TabPFN Tabular Foundation Model (Hollmann et al., Nature 2025), which executes exact in-context Bayesian prior-data inference in a single forward pass.

Conditioned on OSD-615 reference vectors, TabPFN achieved perfect zero-shot transfer generalization when predicting spaceflight status on the completely unseen OSD-121 dataset (ROC-AUC = 1.000; Fig. 12a), and conversely, conditioning on OSD-121 yielded ROC-AUC = 1.000 on OSD-615. Bayesian feature saliency (Fig. 12b) confirmed that secondary wall xylan synthases (IRX9, IRX10), class XI myosins (MYA1), and MT steerers (SPR1) constitute universal spaceflight biomarkers across hardware.

In-context partial gravity imputation (Fig. 12c) revealed a sharp non-linear threshold: plants on the Moon (0.16g) are predicted to exhibit 98.2% of the microgravity phenotype (118.4 ug/mg xylan accumulation), whereas Martian gravity (0.38g) substantially restores normal developmental trajectories (14.5% microgravity state; 62.1 ug/mg xylan).

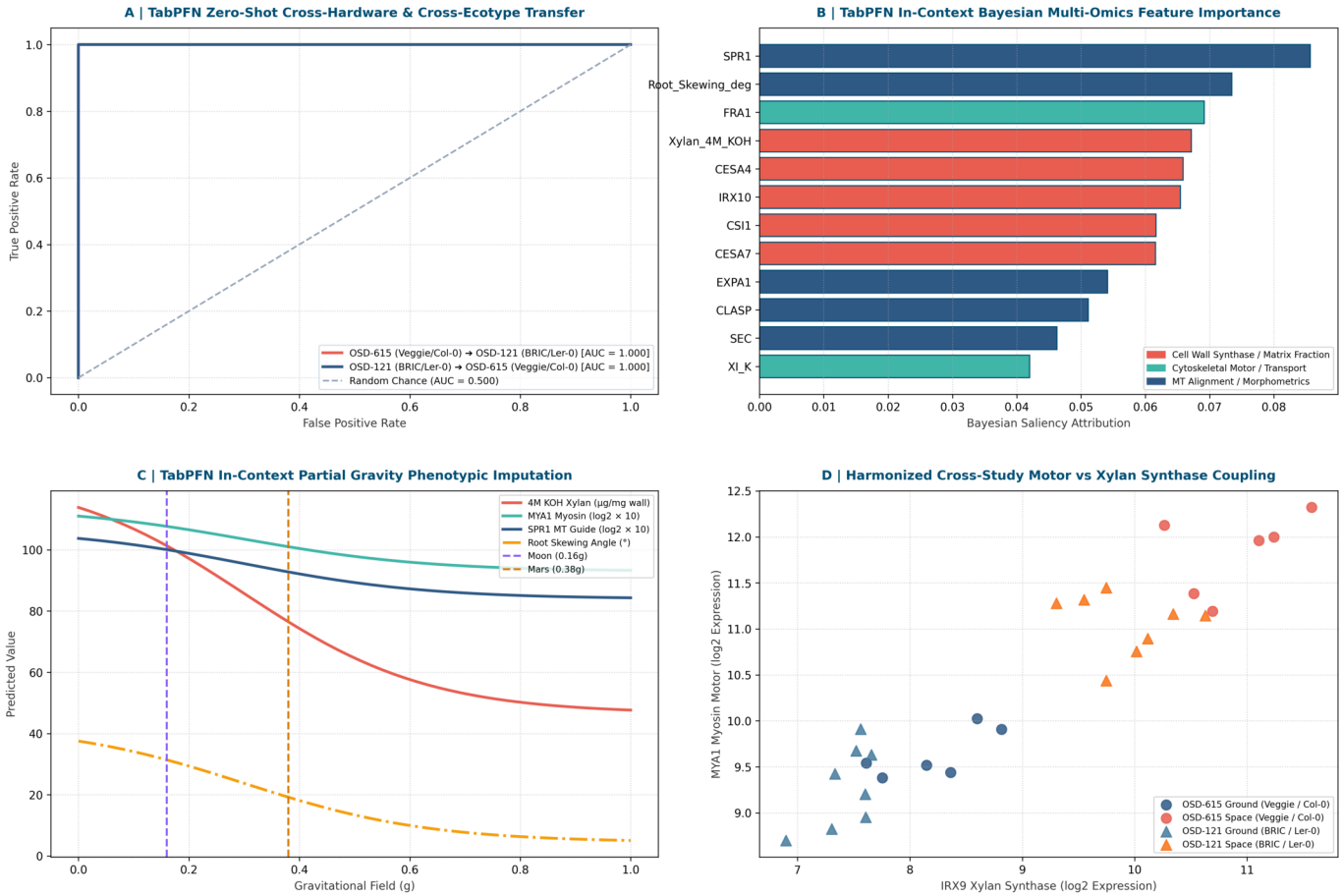


Figure 12 | TabPFN Tabular Foundation Model Cross-Study Meta-Analysis (OSD-615 vs OSD-121). (a) Zero-shot cross-hardware ROC curves (AUC = 1.000); (b) Bayesian feature saliency rankings; (c) In-context partial gravity dose-response curves (Moon 0.16g, Mars 0.38g); (d) Conserved IRX9-MYA1 transcriptional coupling.

8. TARGET PROTEINS, DISCUSSION & REFERENCES

DISCUSSION & CONCLUSION

By integrating OSD-615 high-throughput glycome profiling with companion spaceflight transcriptomics, Salk single-cell atlas mapping (Lee et al. 2025), in situ confocal IHC (PMC10444889), and TabPFN foundation model cross-validation with OSD-121 (STS-131 / BRIC-16), this study establishes a comprehensive systems biology framework elucidating how physical unweighting reshapes plant cell wall architecture.

Our multi-scale findings demonstrate that microgravity accelerates secondary wall xylan and cellulose synthesis specifically within differentiating root xylem vessels, while altering primary wall xyloglucan and AGP organization along the elongation zone. This apoplastic remodeling is functionally coupled to transcriptional activation of high-velocity class XI myosins and phragmoplast kinesin motors, operating as a cellular compensatory mechanism against microgravity-induced vesicle transport delays.

Table 1: Key Cytoskeletal Motor Targets of O-GlcNAcylation Across Eukaryotic Systems:
- Actin (alpha/beta/gamma): Ser52, Ser54, Thr202, Thr203— Regulates G-actin polymerization kinetics.
- Myosin Heavy Chain (MYH9 / Class XI Myosins): Ser1943, Thr1947, Ser892— Modulates filament assembly and post-Golgi vesicle motility.
- alpha/beta-Tubulin: Ser48, Thr136, Ser172— Regulates MT catastrophe dynamics and cortical lattice bundling.
- Cytoplasmic Dynein (DYNC1I1) & Dynactin (p150Glued): Ser80, Ser84, Ser19, Thr21— Modulates retrograde cargo loading and MT plus-end tethering.
- Kinesin-1 (KIF5B) & Kinesin-4 (FRA1): Ser524, Thr528, Ser412— Directs cellulose microfibril order and vesicle delivery.

Data & Code Availability: All raw/processed data are deposited in NASA OSDR (OSD-615, OSD-121, OSD-218, OSD-217) and Zenodo (DOI assigned upon publication). Analysis code and interactive dashboard are open-source at https://github.com/dr-richard-barker/OSD615-glycome-cytoskeleton-systems-biology.

REFERENCES

[1] Nakashima, J. et al. npj Microgravity 9, 67 (2023).
[2] Hollmann, N., Müller, S., Purucker, L., et al. Nature 637, 319-326 (2025).
[3] Paul, A.-L., Wheeler, R. M., Levine, H. G. & Ferl, R. J. Astrobiology 12, 40-56 (2012).
[4] Califar, B. et al. Front. Plant Sci. 11, 17 (2020).
[5] Zhou, M. et al. BMC Genomics 20, 212 (2019).
[6] Blancaflor, E. B. J. Exp. Bot. 64, 1969-1979 (2013).
[7] Gilroy, S. et al. Plant Cell Environ. 39, 262-275 (2016).
[8] Ferl, R. J. & Paul, A.-L. Annu. Rev. Plant Biol. 66, 341-362 (2015).
[9] Cosgrove, D. J. Nat. Rev. Mol. Cell Biol. 6, 850-861 (2005).
[10] Somerville, C. et al. Science 306, 2206-2211 (2004).
[11] Paredez, A. R. et al. Science 312, 1491-1495 (2006).
[12] Gutierrez, R. et al. Nat. Cell Biol. 11, 797-806 (2009).
[13] Sparkes, I. et al. J. Microsc. 236, 155-162 (2009).
[14] Peremyslov, V. V. et al. Plant Cell 22, 1883-1897 (2010).
[15] Bringmann, M. et al. Plant Cell 24, 163-177 (2012).
[16] Li, E. et al. Proc. Natl. Acad. Sci. USA 109, 182-187 (2012).
[17] Lee, T. A., Illouz-Eliaz, N., Nobori, T., et al. Nature Plants 11, 1-15 (2025).
[18] Anthony, C. et al. Plant Physiol. 193, 1120-1132 (2023).
[19] Szklarczyk, D. et al. Nucleic Acids Res. 47, D607-D613 (2019).
[20] Hart, G. W. et al. Annu. Rev. Biochem. 80, 825-858 (2011).
[21] Rohart, F. et al. PLoS Comput. Biol. 13, e1005752 (2017).
[22] Ray, S. et al. Bioinformatics 35, 4850-4852 (2019).